Nucleation-enhanced condensation and fast shedding on self-lubricated silicone organogels

Nicolas Lavielle, Daniel Beysens, Anne Mongruel

Nucleation-enhanced condensation and fast shedding on self-lubricated silicone organogels

Nicolas Lavielle*, Daniel Beysens and Anne Mongruel

Physique et Mécanique des Milieux Hétérogènes, CNRS, ESPCI, PSL Research University, Sorbonne Université, Université Paris Cité, 75005 Paris, France

Corresponding author: nicolas.lavielle@espci.fr

Keywords: silicones, liquid-infused surfaces, lubricant, dropwise condensation, nucleation, coalescence, shedding.

Abstract:
A cross-linked silicone elastomer swollen in silicone oil releases at its surface a thin oil layer, whose thickness slowly increases with time as a consequence of surface energy minimization and residual crosslinking reactions within the polymer matrix. Here, we tune and characterize this oil layer thickness (between 0 and 5 μm) in order to show its quantitative influence on the physical mechanisms at play during water condensation: droplet nucleation and growth, coarsening by menisci-mediated coalescences, and droplet shedding by gravity. We show that a continuous nucleation is at the origin of enhanced condensation. Spontaneous replenishment of the oil layer occurs thanks to the storage of oil in the bulk of the swollen elastomer, allowing the same sample to be used for repeated long-lasting condensation experiments.

1. Introduction

Dropwise water vapor condensation on a surface cooled below the dew point temperature is advantageously used by nature[1–3] or in industrial processes, with applications ranging from heat management[4], power generation[5], desalination[6] to water harvesting[7–9]. Efficient heat transfer and atmospheric water vapor harvesting both require optimal surface properties to achieve: (i) high nucleation rate for large condensed water volume, (ii) low contact angle hysteresis (CAH) to enhance droplet mobility, (iii) enhanced droplets growth to reach rapidly the critical droplet size for gravity shedding.

A well-known class of materials that meets the above requirements is concerned with liquid-infused surfaces (2D-LIS)[10,11], which are composed of a nano/micro-textured surface impregnated with a layer of a lubricant of low vapor pressure; lubricant is chosen to preferentially wet the texture and to exhibit non-wetting and low hysteresis properties with water[12,13]. 2D-LIS have shown stable operating conditions during condensation, unlike super-hydrophobic surfaces, which can lose their repellency or non-adhesive properties when condensation yields droplets in the Wenzel regime[14,15]. The lubricant layer is the key-element that gives to 2D-LIS favorable properties for water condensation. First, the deformation of the liquid surface decreases the energy barrier of nucleation[16,17] . Then, if the spreading coefficient is positive, nucleated water droplets are cloaked by the lubricant layer

and are immersed in oil until their size becomes larger than the oil thickness[18]. At that time a wetting ridge (i.e. a meniscus) forms at the base of the emerged droplets. Wetting ridges lead to attractive capillary forces due to overlapping menisci bringing distant droplets to contact and hence, to coalesce[11,19,20]. Meniscus-mediated coalescence events not only lead to a rapid droplet growth until the critical size for shedding is reached, but also generate new nucleation on the fresh surface left free by these events[19]. In addition, the oil layer suppresses or at least substantially lowers the pinning of the contact line on the solid surface. This ultralow CAH promoted by the oil layer induces a rapid shedding of the condensed droplets at low critical size[21,22]. These effects are valid for thin oil layers of relatively low viscosity, whereas condensation on liquid baths or high viscous thin liquid layer limit droplets coalescence[18,19,23].

A major drawback of 2D-LIS, however, is the finite amount of lubricant available on its surface. Water condensation inevitably leads to lubricant depletion and loss of the materials properties[24,25]. Oil depletion from the solid surface occurs by the redistribution of the oil layer around the moving droplets[19]. On an inclined surface, oil is drained by droplet shedding [26]. Materials or systems have been designed to address the issue of oil depletion, minimizing the oil loss using nanostructured tubes[26] or maximizing the interaction between lubricant and solid surface[27]. Despite these efforts, the materials fail over time. Another approach consists in the continuous replenishment of oil from an external reservoir, e.g. using rotational oil brushing[28], but this strategy requires energy input and is not applicable for variable material geometries.

In this study, we use a so-called organogel or 3D-LIS[25], which differs from the 2D-LIS described above in two ways. First, the lubricant is infused within the bulk matrix of a 3D crosslinked elastomer network, which is used as a lubricant reservoir. Second, the lubricant migrates from the bulk of the elastomer to the elastomer surface in order to generate a slippery liquid surface layer, which is continuously replenished[29,30]. These 3D-LIS have been used in a number of applications in the medical field, exploiting their bacterial antiadhesive and antifouling properties[29,30]. To our knowledge, exploring their potential in water condensation applications is novel

It is anticipated that superior performances will be granted to iPDMS compared to 2D-LIS materials by the following distinct features: (i) The fabrication is easy and scalable, in particular surface micro-structuration is not needed, (ii) oil is present as a reservoir in the elastomer matrix, (iii) the thickness of the oil layer at the iPDMS surface continuously increases over time, and (iv) replenishment of this oil layer occurs following depletion.

This paper is organized as follows. After characterizing the evolution of the lubricant layer thickness, we take advantage of the slow kinetics of this process to perform condensation experiments at various stages of the layer growth. We show that the value of this lubricant layer thickness has a major quantitative influence on the physical processes at play during dropwise condensation on a lubricant surface, i.e. the nucleation process, the growth of a single droplet, the menisci-mediated drop coalescences and the shedding of droplets. In particular, we quantify the continuous nucleation process arising mostly in the first moments of the condensation, and show that it adds to the classical diffusion-limited droplet growth to increase the collected water volume. Finally, the long-lasting condensation performance of the iPDMS is demonstrated by repeated cycles of oil depletion by condensation followed by oil release on the same sample.

2. Materials and Methods

We selected a silicone elastomer (PDMS, crosslinker to base resin mass ratio of 1/20) and a liquid silicone oil (methyl-terminated linear PDMS chains, 10 cSt) with very close solubility parameters. Swelling the PDMS elastomer in the silicone oil results in a silicone oil-imbibed PDMS organogel, hereafter denoted as iPDMS or self-lubricated silicone[29,30]. The critical surface tension of wetting of crosslinked PDMS in air is 22.7 $mN.m^{-1}$, whereas the surface tension of the selected silicone oil (methyl-terminated) is 20.1 $mN.m^{-1}$ [31,32] at room temperature. Thus, an oil layer "spontaneously" forms at the iPDMS surface to minimize surface energy. To obtain a substantial oil layer at the surface of the PDMS material (up to a few micrometers), a crucial point is to infuse oil *after* PDMS curing. Indeed, if the lubricant infusion is performed *before* curing[33], or when un-crosslinked chains are extracted from the PDMS by the deposition of water droplets[34], the amount of released oil is not significant enough for an oil wetting ridge to be formed around the droplets, and hence for capillary attractive interactions to proceed between droplets.

Swelling ratio (*SR*), defined as the ratio of the mass of the imbibed liquid (silicone oil) to the initial mass of the solid (crosslinked PDMS), depends on the chemistry and viscosity of the oil and on the crosslinking density of the elastomer matrix[30]. Note that the choice of a 10 cSt oil viscosity was dictated to fulfil contradictory requirements. Lower oil viscosity leads to oil evaporation, higher oil viscosity leads to a smaller *SR*, delay in drops coalescence and a potential slower release of oil at the iPDMS surface. In addition, the cross-linking ratio of 1/20 was chosen to infuse a large quantity of oil (high *SR*), while exhibiting mechanical properties in the range of usual elastomers.

For achieving the desirable interactions between water droplets, lubricant layer (silicone oil) and elastomer (PDMS), the different interfacial energies must follow some requirements. Silicone oil will cloak condensed water droplets as the spreading coefficient (S_c) of the silicone oil to the water droplet is positive. $S_c = \gamma_{wa} - \gamma_{oa} - \gamma_{ow} > 0$, with γ_{wa} the interfacial energy for water-air (72 $mN.m^{-1}$), γ_{oa} for oil-air (20.1 $mN.m^{-1}$) and γ_{ow} for oil-water (36 $mN.m^{-1}$)[35]. Upon condensation, the characteristic time for droplet cloaking is several orders of magnitude smaller than the typical time for droplet growth, which indicates that the condensed water droplets remain cloaked (by a film of tens of nm) during the whole process of condensation[18]. Cloaking will ensure the existence of attractive capillary forces between droplets when menisci overlap. Droplet mobility for coalescence events and droplets shedding will be insured in this system as a silicone oil interface will be present in between water and solid PDMS surface since $\gamma_{sw} - \gamma_{so} - \gamma_{ow} > 0$ (interfacial energies of solid-water 41 $mN.m^{-1}$ [36], oil-water 36 $mN.m^{-1}$and solid PDMS- silicone oil ≈ 0 $mN.m^{-1}$) .

Preparation and characterization of iPDMS

To fabricate the PDMS gel, 2 parts hydrosilylation-cured PDMS (Sylgard 184) from Dow Corning were mixed with the ratio 20 for the mass of the PDMS resin to the mass of the cross-linker (*1/X*). 20 g of the mixture was poured in polystyrene Petri dishes to obtain a

material thickness of around 2 mm, de-gassed for 1 h. in a vacuum chamber and cured overnight in an oven (Binder) at 70°C. For iPDMS preparation, PDMS pieces of 2×2 cm^2 (for optical microscopy experiments) and 9×9 cm^2 (for measurement of the oil thickness and climatic chamber experiments) were cut and immersed in a bath of silicone oil (linear methyl-terminated PDMS oil, of dynamic viscosity 10 cSt, and density 968 kg/m3, purchased from Sigma Aldrich). After 2 weeks in oil to ensure swelling equilibrium, the iPDMS samples were washed under flowing water to remove the silicone oil from the surfaces. The Young modulus of iPDMS samples is 480 kPa[30]. iPDMS samples were weighted (balance Sartorius Entris, accuracy of 1 mg) prior and post-swelling in the silicone oil to measure the swelling ratio (*SR*) and verify swelling equilibrium[30]. In order to evidence the residual crosslinking in PDMS, the material was left from 1 day (usual curing time) to 30 days at 70°C (under curing) and swelling in silicone oil was performed at different times. Figure 1a shows a power law decrease of *SR* with curing time with exponent ~ - 0.1, confirming the residual crosslinking reactions within the polymer matrix. The swelling ratio is known to linearly decrease with increasing crosslinking density[30]. At room temperature, this effect is much slower but is sufficient to continuously expulse the imbibed oil.

In order to measure the evolution of the oil layer thickness, a swollen iPDMS piece of 9×9 cm^2 was removed from the oil bath at swelling equilibrium. The excess of oil was removed, then the sample was washed under water at different times (from 2 h. to 112 days) to remove the released silicone oil from the iPDMS surface and then weighed. Oil thickness was calculated from the mass loss (measured with a precision of ± 1 mg), assuming a uniform oil layer thickness and an equivalent release from the top and bottom surfaces. To note, the mass loss upon washing was at least of an order of magnitude higher than the balance precision accuracy of 1mg, corresponding to a layer thickness of ~ 0.1 µm.

Figure 1b gives the evolution of oil layer thickness $h(t)$ released from iPDMS samples at room temperature. Here, the origin of time is taken at the moment of first washing of the sample just after withdrawn from the oil bath. The oil film thickness, *h*, reaches 10 µm within 4 weeks. One observes an initial power law in time with exponent ½ (Figure 1b), indicating a diffusive release from the PDMS matrix. However, the release of oil weakens with time and does not follow the initial kinetics beyond 10 days. This is possibly due to a decrease of the amount of the further crosslinking reactions over time, and supported by the weak power law dependency found in Figure 1a. Note that a diffusive behavior was also found for oil imbibition in the crosslinked network [30]. It is important to note that the evolution of *h* presented on Figure 1b is representative only for the system under study: PDMS (1/*X*= 20) and methyl-terminated silicone oil of 10 cSt.

It is thus possible to tune the oil layer thickness of iPDMS samples by varying the sample resting time after first washing, and using the graph of Figure 1b. The same iPDMS sample was re-used by re-washing it at time t_w. In that case the amount of oil previously released (from time *t* = 0)) has to be subtracted, since it is a continuous process. The evolution of the new oil layer thickness, $h_{new}(t)$,at $t > t_w$ is then: $h_{new}(t) = h(t) - h(t_w)$. It is therefore essential to be aware of the material history (cleaning events) in order to correctly evaluate the oil layer thickness. This procedure enables to control extremely small values of oil layer thickness during the diffusive oil release. However, under some circumstances, more oil can be expelled. This first occurs when condensed water is present on the surface. Water indeed changes the surface energy by the presence of an oil film between the water drops and the

"solid" surface. In order to minimize the surface energy (see above), iPDMS extracts oil from its reserve. The cloaking process of water drops therefore "pumps" oil from the matrix[33,34]. Thanks to condensation, a minimum oil layer will be then always present. Additionally, there is also a temperature factor which leads to expel more oil. When the temperature of iPDMS is lowered, a weak but actual reduction in volume also gives rise to oil release**.**

Figure 2 gives the static contact angle (*CA*) and the contact angle hysteresis (*CAH*) of water droplets on PDMS and iPDMS with different oil layer thickness, ranging from 40 nm to 5.4 µm. The measurements were made using a goniometer (Kruss, DSA 25S), by the deposition of 1µL ultra-pure water droplets on the samples. Three samples per measurement were used. All materials have essentially the same apparent static contact angles, around 100°. With an oil layer thickness of only h = 40 nm, the *CAH* is drastically reduced from around 60° for PDMS to ≈ 5° (for iPDMS-0.04 µm). When h > 250 nm the *CAH* is further decreased to its minimal measurable value, ≈ 1°. Therefore, while an oil layer thickness of 40 nm is not sufficient to reach the minimal value of the *CAH,* 250 nm are sufficient to suppress droplet pinning and ensure ultra-low contact angle hysteresis.

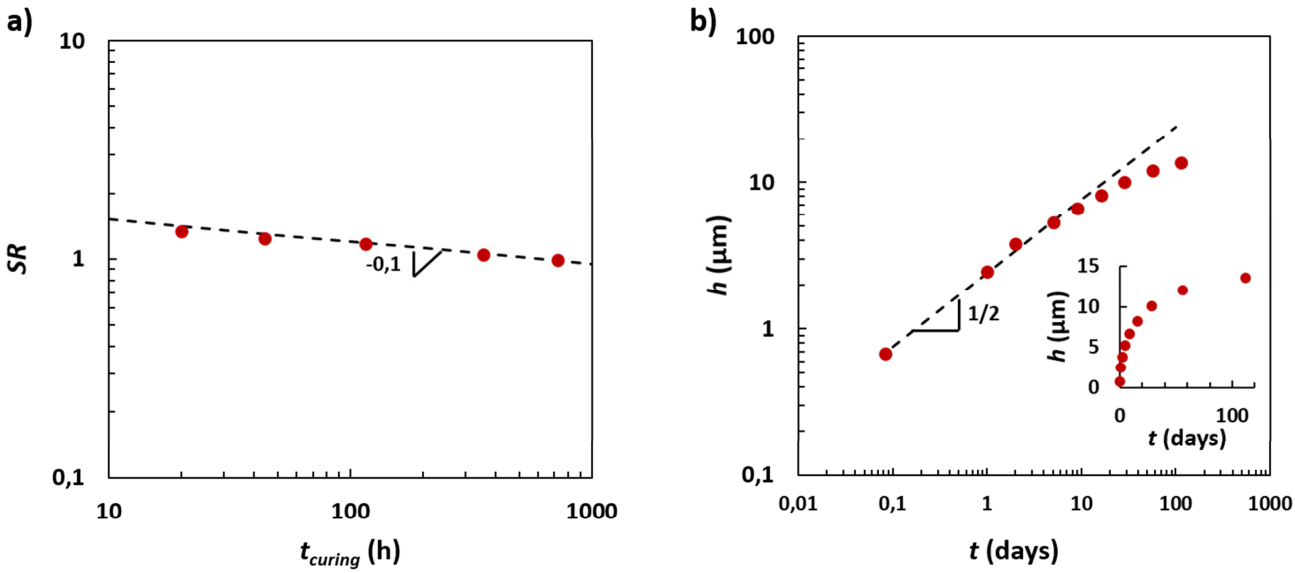

Figure 1: Evolution of iPDMS (log-log plots)**:** a) Swelling ratio (*SR*) as a function of curing time (t_{curing}) revealing residual crosslinking reaction within PDMS matrix. b) Evolution of silicone oil layer thickness (h) with time. The origin of time is taken at the redrawing from the oil bath. (Inset is the same plot in linear scale)

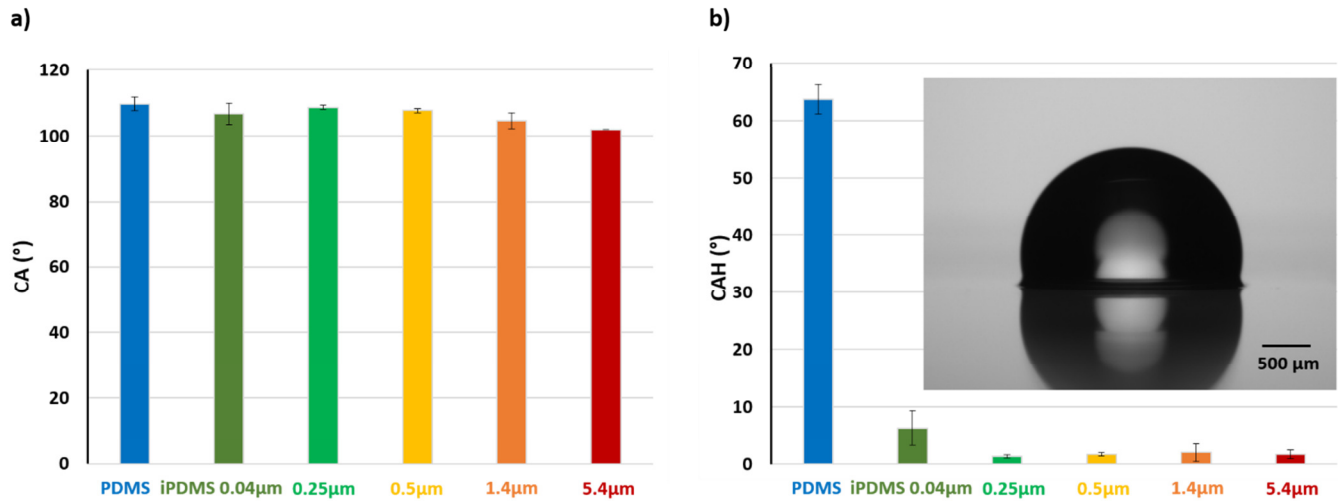

Figure 2: **Wetting properties:** Static contact angle (*CA*) and contact angle hysteresis (*CAH*) of water on PDMS and iPDMS with different oil thickness ranging from 40 nm to 5.4 µm.

Observation under optical microscope – droplets growth and condensed water volumes

Water condensation was performed on 2×2 cm^2, horizontal PDMS or iPDMS samples in a home-made mini-climatic chamber mounted on an optical microscope (Leica DMRXE) equipped with a camera (Imaging Source, DFK 23U445). The sample is placed on a horizontal electrolytic copper plate in contact with a Peltier element. The chamber is sealed by a Plexiglas cover with a top sealed glass slide for optical observation. Air saturated with water vapor is obtained by bubbling air in a bath of ultrapure water and injected through two inlet nozzles placed in front of each other at the sides of the mini-chamber in order to obtain a stagnation flow at the center. The Peltier element is fed by a current of 2 V and 0.5 A (generator, Sodilec SDRI 205). The hot side is cooled by a flow of water at 10°C (Heto CBN 8-30 and HMT 200) to ensure that the surface temperature of the copper plate is constant and equal to 4°C. Surface temperature of the copper plate is monitored all along the experiments by using a thermocouple sensor and the software Picolog. The sample surface temperature is 1 °C higher than the surface of the Peltier. The humid air injected in the mini-chamber has a relative humidity of 90% and its temperature is equal to room temperature ≈ 20°C. In these experimental conditions, the sample surface temperature is far below the dew point temperature (16°C in these conditions) to remove the influence of unwanted temperature variations and ensure reproducible condensation. For each condensation experiment, the temperature of the copper surface is first driven to 4°C. At this point, humid air flow is sent into the chamber, time is set to zero and observation begins. A scheme of the experimental microscope setup can be found in Scheme 1a.

The ICCapture software was used for the video and images sequence acquisition. Videos at 15 FPS were used to study the growth of single droplets (3 droplets per measurement) and images sequences (1 image per s, for 1000 s) for the condensed water volumes (3 samples per measurement). The ImageJ software was used to analyze the images. The analysis consists in detecting drop areas on the images by an appropriate threshold and setting a

minimum detection limit at 10 μm^2. A projected drop radius is derived from this area, corresponding to the radius of a circular disk of same area. On iPDMS, the drop projected area is indeed circular, whereas on PDMS there is a small departure from circularity due to contact line pinning. The droplet radius and droplet volume were calculated from this apparent projected radius, using a 100° contact angle. Note that the adjustment of the threshold is critical to ensure that the wetting ridge is not included in the detected drop area (see Figures S4 and S5). Note also that for a small number of droplets, detected areas may also include cluster of non-coalesced droplets (see Figure S4). The apparent projected radius derived from this procedure is thus overestimated when both effects are significant, i.e. for large oil layer thickness and short experimental time. Using simple geometry, the ratio between the apparent volume and the actual volume can be estimated. A maximum ratio of 1.3, leading to a maximum uncertainty of 30% was found in the case of the highest oil thickness and at early times of condensation. A 20% maximum uncertainty was observed in the other cases.
The same microscope and image analysis software were used for the evaporation experiments, performed by depositing 0.5 µL of ultra-pure water on the studied samples at room temperature.

Condensation in climatic chamber – Collected water volumes

Condensation was performed on 9×9 cm^2 samples attached to a vertical electrolytic copper plate set in a climatic chamber (Weiss, WKL 100) with controlled temperature (30°C) and relative humidity (70%) for all experiments. The copper plate was in contact with a Peltier element fed by a current of 3.8 V and 2.5 A (generator, TTi QPX 1200L) and a flow of cooled water at 10°C (Julabo F250) in order to maintain the surface temperature of the copper plate at a constant temperature of 16°C, well below the dew point temperature (23°C in these conditions). The surface temperature of the Peltier was monitored by using thermocouple sensor and the software Picolog. The temperature of the sample was measured at 17°C. Condensation was studied from near and far fields observation by using two cameras (Imaging Source, DFK 23U445). Shedding water droplets were collected by a hydrophilic stamp set within ~ 1 mm from the sample bottom and weighed all along the experiment (Denver Instrument, SI-603, 1mg accuracy). The collected water mass was recorded every 2 s by using a MATLAB code. For each condensation experiment, air in the climatic chamber was firstly set to the desired temperature and RH. Then the copper surface temperature was cooled to the desired temperature (16°C). When this temperature was reached, the sample was placed on the surface within a few 10 s. and time was set to zero for mass measurements and drop pattern visualization. Experiments were performed during 4 hours. The iPDMS samples were weighed prior and post experiment to measure the oil loss and calculate the mass percentage of oil in the collected water. To test the robustness of the iPDMS material and detect possible aging effects, the same sample was used for all the experiments in the climatic chamber. A scheme of the experimental setup of the climatic chamber can be found in Scheme 1b.

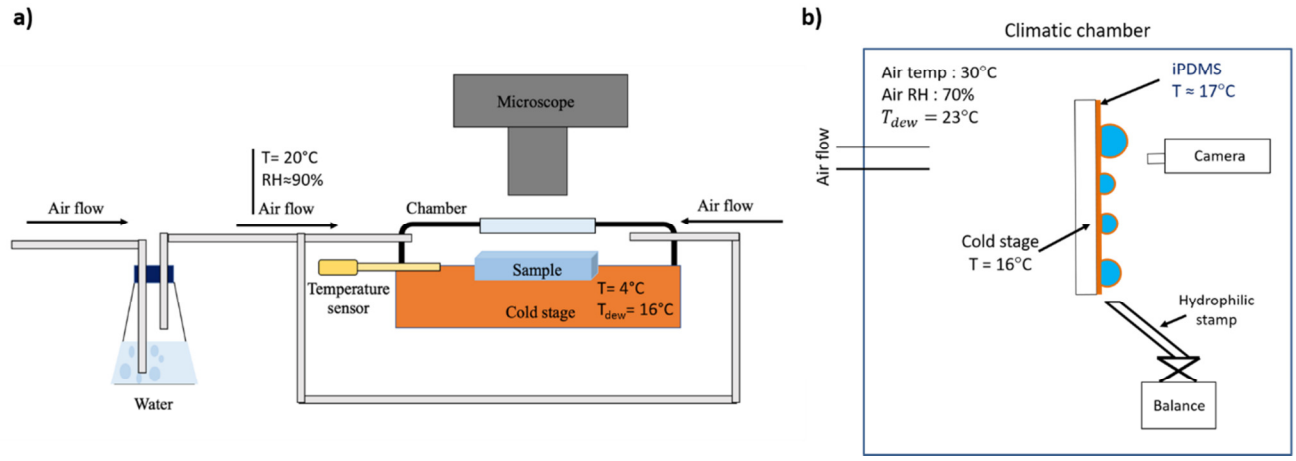

Scheme 1: Experimental setups: (a) Condensation under microscope, (b) Condensation in climatic chamber.

3. Results and discussion

Figure 3 illustrates how the presence of the oil layer on iPDMS fundamentally changes the mechanisms of droplet nucleation and growth during water condensation compared to bare PDMS. Optical microscope images are taken during the first 100 s of water condensation on horizontal surfaces for PDMS and iPDMS (h= 2µm). At a given time, major differences are seen in terms of droplets size and size distribution. On PDMS, the breath figure evolution is typical of condensation on a soft material [17,33]. It shows high nucleation density as related to the decrease of the air–water interface area when compared to a rigid surface, which compensates for the energy increase related to the elastic deformation and the increase of the substrate-water interface area. High droplet pinning is observed due to the triple line contact deforming the surface, leading to delayed coalescences. As a consequence, re-nucleation is hampered by the presence between drops of water molecules concentration profile that overlap. By contrast, after only 5 s, one can already observe on iPDMS the presence of large droplets or clusters of coalescing droplets, leaving large surfaces of oil available for re-nucleation. This rapid coarsening is typical of attractive capillary attraction between distant droplets. Movies S1 (PDMS) and S2 (iPDMS) display the water condensation dynamics presented in Figure 3, and show the striking difference in the nucleation, mobility and coalescence of droplets on these two substrates during the first 100s of condensation. These observations confirm that our iPDMS samples satisfy the required oil-water interactions as discussed in the introduction. The significant thickness of the oil layer leads to unbalanced capillary interactions between menisci that drive distant droplets to each other. The high mobility of droplets is achieved through ultra-low CAH. These combined effects promote early coalescences of droplets (coarsening), which free up continuously the oil surface for new nucleation. In the following, we investigate in more details the growth of a single droplet by different mechanisms. We also quantify the effect of the oil layer thickness on the droplets size distribution.

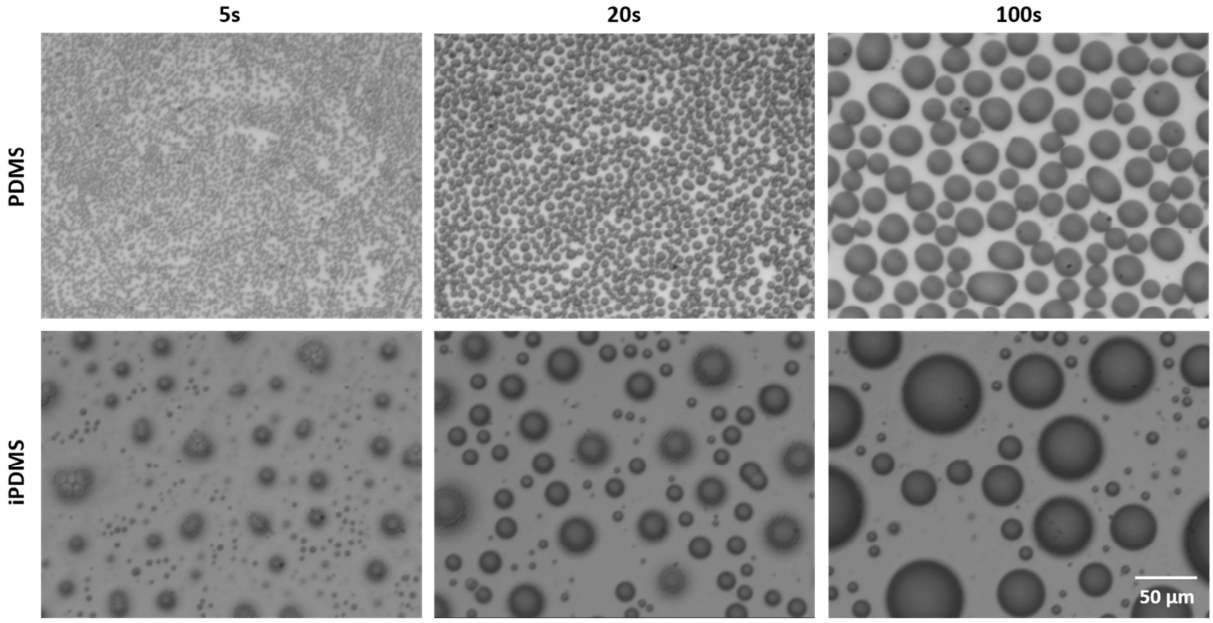

Figure 3: Water condensation on PDMS and iPDMS (*h* =2 µm): Optical microscope images of condensed water droplets on horizontal surfaces for PDMS and iPDMS at 5, 20 and 100s after the beginning of condensation.

3.1. How water droplets grow on iPDMS

Growth of droplets on a solid or liquid surface after nucleation is classically described by a diffusive growth due to a water molecules concentration profile around them and coalescence events[37-39]. Three typical growth laws can be found. (a) Initially, when droplets are still sufficiently apart such as the concentration profiles do not overlap, the drop cap radius *r* obeys the power law evolution $r \sim t^{1/2}$. (b) Later, when the concentration profiles above the drops merge into a mean profile parallel to the surface, the growth exponent becomes 1/3 such as $r \sim t^{1/3}$. (c) When coalescences between drops take place, growth (b) is unaffected between coalescences, the latter only accelerating the average drop pattern radius as $\langle r \rangle \sim t$. Meanwhile, the number of coalescences *N* undergone by a drop evolves with time as $N \sim \ln(t)$[40,41].

(i) Individual droplet growth by direct condensation

While the process of nucleation, cloaking and coalescence of water droplets inside an oil layer (immersed state) has been already analyzed, the process of the further growth of cloaked drops emerging from the oil layer is still unclear. Concerning condensation on PDMS (no oil film), we measure a power law dependence with exponent ~ 1/3 , characteristic of stage (b) (Figure S1). For iPDMS, we observe the same power law (Figure 4a, with coalescence events indicated by arrows). The inset 1 of Figure 4a shows the same evolution with the contribution of the coalescence events subtracted. The exponent 1/3 indicates that the growth of the cloaked droplet is still governed by the diffusion of water molecules in air, as for the PDMS drops. A diffusive permeation of water molecules through the cloaking layer

is therefore probable and consistent with the fact that silicones are highly permeable to water vapor[42].

(ii) Growth by meniscus-induced attraction and coalescence

The presence of a wetting ridge deforms the oil layer interface between the condensed water droplets and leads to attractive capillary interactions when oil menisci overlap[11,19]. When condensation is stopped, the attractive motion of droplets is suppressed, indicating that unbalanced capillary interactions are sustained by condensing droplet growth. The Inset 2 of Figure 4a depicts a typical plot of the number of coalescence events involving a single droplet during its growth on iPDMS and PDMS. On PDMS, the expected behavior $N \sim \ln(t)$ is found. For iPDMS, a much larger number of coalescence events is seen when compared to PDMS, with a significant impact on droplet growth. Two regimes are found for the number of coalescences undergone by a single droplet. In the first 5 seconds of observation of droplet growth, a linear evolution $N \sim t$ is observed. It is then followed by the power law $N \sim t^{1/3}$. The first linear evolution can be understood by the linear increase of the density of nucleated droplets with same size. The second evolution is more difficult to evaluate and is beyond the scope of the present paper.

(iii) Growth of re-nucleated droplets

To further explore the mechanism of droplet growth on iPDMS, we study the evolution of the radius of a droplet after nucleation of new droplets on a region left free by the coalescences. Figure 4b presents the radius evolution of an isolated single droplet (average radius of 3 different droplets) on PDMS and iPDMS. A power law evolution $r = (At)^{1/2}$ is found, corresponding to the stage of growth (a). The amplitude constant *A* is a function of the supersaturation at the condensing surface, the diffusion coefficient in air of the vapour molecules and the drop geometry[39,41] (c.f. Supplementary Information). We found a value for *A* (Figure 4b) almost 4 times larger for iPDMS as compared to PDMS (A_{iPDMS} = 2.25 µm^2.s^{-1}, A_{PDMS} = 0.59 µm^2.s^{-1}). However, the theoretical calculation[39,42] based on geometrical arguments (using the advancing contact angle) gives a ratio of only 1.4 (c.f. Supplementary Information for the calculation of the amplitude constants and their ratios). The same experiment was performed on silicon wafer (Si), and the results are presented in the inset of Figure 4b. The amplitude constant on silicon wafer is A_{Si} = 1.93 µm^2.s^{-1}; it is smaller than A_{iPDMS} but should theoretically be almost 2 times larger. The unexpected large value of A_{iPDMS} shows that the diffusion-permeation of water vapor is not the only growth mechanism. In addition to the latter mechanism, another process, the direct incorporation of nucleated droplets (not visible under a microscope), occurs at the vicinity of the growing droplets or on the cloaking layer[18]. During their haphazard motion in the oil film, nucleated droplets coalesce with a large drop. One notes that it is a process similar to the incorporation at the surface of the emerged drop of the Brownian water vapor molecules in air. It thus should lead to a concentration gradient of nucleated droplets around the drop and to a drop growth law also in $t^{1/2}$.

(iv) Evaporation of deposited droplet on iPDMS. In order to elucidate the role of the cloaking layer in the growth process, the evaporation of a single 0.5 µL water droplet was studied

once deposited on the three surfaces (iPDMS, PDMS and Si). The plot of the droplet radius (from disappearance to deposal), is reported in Figure S2. Diffusive evaporation was found with a scaling exponent of 1/2 for the 3 surfaces, with respective amplitude constants, E_{iPDMS} = 324 µm^2.s^{-1}, E_{PDMS} = 625 µm^2.s^{-1}, E_{Si} = 1369 µm^2.s^{-1}. The total evaporation time for 0.5 µL droplets on iPDMS, PDMS and Si were respectively 1100, 950 and 530 s). For similar conditions of evaporation, the amplitude constants differ only by the drop geometry (using the receding contact angle; c.f. supplementary notes). The calculated E ratio[42] between iPDMS and PDMS is similar to the experimental value. However, the calculated E ratio between iPDMS and Si (and the ratio between PDMS and Si) is two times larger than the experimental one, which is in consistent with the fact that permeation across the cloaking layer slows down the droplet growth. These results confirm that a cloaking oil layer (case of iPDMS) or a cloaking layer of un-crosslinked chains (case of PDMS)[34], although impacting the diffusion of water molecules when condensation or evaporation proceeds, remains permeable to these water molecules.

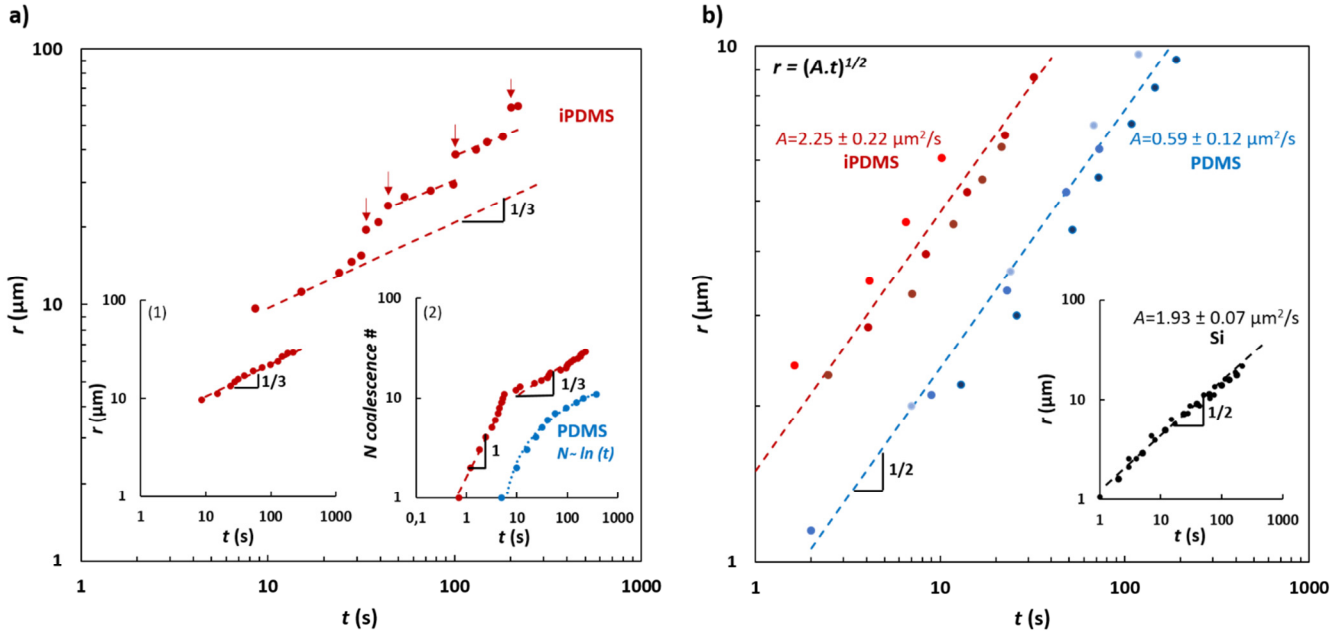

Figure 4: Droplet growth on iPDMS horizontal surfaces: a) Typical evolution of the cap radius r of a single droplet on iPDMS (coalescence events are indicated by red arrows). Inset 1: Same plot with coalescence events subtracted. Inset 2: Number of coalescence events for a single droplet on iPDMS and PDMS. b) Radius evolution of a single droplet (mean of 3 droplets) from nucleation to first coalescence (in a fresh region left by the coalescence of two major droplets) on iPDMS and PDMS. Inset: Same experiment and plot for condensation on a silicon wafer. (t=0, corresponds to the moment when the droplet becomes visible)

3.2 Influence of oil thickness on condensation

In this section, the images of condensation under microscope are analyzed (see Material and Methods) in terms of distribution of the droplets radius. The smallest projected droplet radius resolvable by the microscope is 2 microns. This size is much larger than the size of a nucleus but is on the order of the oil layer thickness. On iPDMS, smallest detected droplets

have just emerged from the oil layer, after growing inside the oil layer as discussed previously.

(i) Continuous nucleation and meniscus droplet coalescences

Figure 5 presents the evolution of the size distributions of the projected drops radius *r* (number of droplets, *N*, of radius *r,* measured by steps of 20 microns) in the first 1000 s of the condensation experiment for PDMS and iPDMS with various initial oil layer thicknesses. Oil thickness *h* was controlled using the results of Figure 1b. For PDMS (Figure 5.a), contact-triggered coalescences leads to a one-peak distribution with gradual displacement of this peak towards larger droplet radius. The bimodal distribution characterizing a small number of new nucleation events appears late in the process (1000 s).

By constrast with PDMS, Figure 5b,5c and 5d highlights the coarsening process arising on iPDMS, characterized by a continuous increase of the number of large droplets (larger than 80 µm) from the beginning of the observations, resulting from meniscus-mediated coalescences between distant droplets. Concurrently, a continuous presence of small droplets (persistent peak at 20 µm) is observed on iPDMS, which is the signature of a continuous nucleation process on the oil surface left free by the meniscus-mediated coalescences. Continuous nucleation and meniscus-mediated coalescences both need a minimum oil layer thickness to proceed. Starting from a given initial oil thickness h, inhomogeneous redistribution of oil thickness occurs around the coalescing droplets: oil accumulates in the wetting ridges of the larger droplets whereas it is depleted between them. It follows a gradual decrease of the meniscus-mediated coalescences with time, hence a decrease of the free space available for continuous nucleation, and the number of small droplets decreases accordingly (Figure 5b). Conversely, for a larger initial oil thickness, the number of meniscus-mediated coalescence events is larger, and hence, a larger amount of small droplets are nucleated at a given time (Figure 5c and 5d).

Interestingly, for the iPDMS with the smallest initial oil layer (0.25 µm) the number of small droplets remains quasi-identical from 500s to 1000s, which indicates the existence of a minimum (threshold) lubricating oil layer thickness to sustain the meniscus-mediated coalescences. Indeed, the minimization of surface energy implies the existence of a minimum oil layer thickness between the water droplets and the solid PDMS surface, whose thickness is difficult to assess or estimate. Figures S3 presents the normalized size distributions of the plots of Figure 5 and evidences the formation of larger droplets with an increase of oil thickness, as observed on Figure 3 and 5.

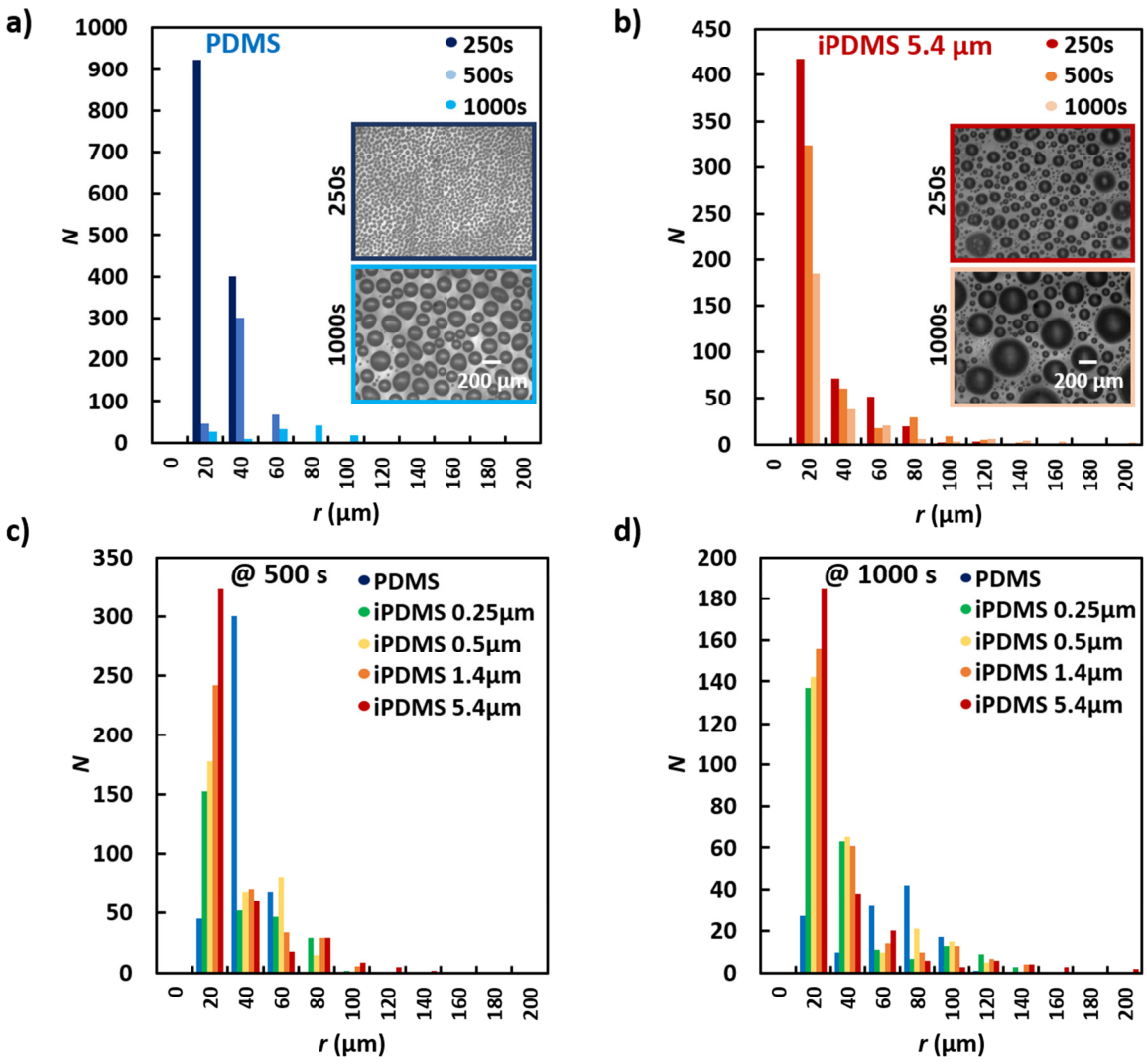

Figure 5: Radius distribution of condensed water droplets on horizontal surfaces: Evolution of the number of droplets, *N*, of radius *r*, for (a) PDMS and (b) iPDMS with 5.4µm oil thickness (Inset represents the optical microscope images of condensed water droplets for PDMS and iPDMS at 250s and 1000s). Size distribution for PDMS and iPDMS with various oil thicknesses at (c) 500 s and (d) 1000 s. (Step of 20 µm)

Condensed water volumes and condensation rates are calculated from the projected droplets radii, assuming droplets with contact angle of 100°. Figure 6a shows the evolution of *Vs*, the total volume of condensed water per unit surface (in µm) as a function of time for PDMS and iPDMS with different oil thicknesses.

At the beginning of condensation, the condensed volumes on iPDMS increase faster than on PDMS, and this increase is more pronounced and lasts longer when the oil layer is larger. As a result, after 20 s of condensation, almost ten times more water is condensed on iPDMS with h = 5.4 µm as compared with PDMS. After 200s, however, all volumes follow a parallel evolution. At 1000 s, the condensed water volume on iPDMS with h = 5.4 µm is thus only twice as compared with PDMS. This shows that the continuous nucleation process taking place in the first seconds of condensation adds to the droplet growth by diffusion. The net

effect is a larger condensed volume. The increase of the oil thickness increases the duration of droplet submergence, allowing continuous nucleation at the oil-air interface to be longer maintained. This longer-lasting continuous nucleation period is evidenced in Figure 5. Figure 6b gives the evolution of the condensation rate ($\tau = dV_S/dt$, in mm.h^{-1}) for PDMS and iPDMS data of Figure 6a. It confirms that the condensation rate is higher with an increase of *h* in the first 300 s of the condensation experiments. After this time period, all surfaces exhibit similar condensation rate. One might think that the continuous droplet nucleation at the oil surface, at the source of the enhanced condensation, should induce a gradient of water molecules in air, similar to what is observed with drops on a solid, and limits the condensation rate. However, nucleation is involved with concentration fluctuations and the subsequent growth of micro-droplets before their submergence occur only during a very short time (1ns -1ms)[18]. During this time, a steep concentration gradient should indeed form, whose typical extent scales with the droplet radius[7,39]. The rapid submergence of the micro-droplets and the fact that nucleation proceeds from fluctuations thus prevent the formation of a steady gradient. These characteristics explain why this nucleation-triggered condensation can be much enhanced when compared with the classical diffusion-limited condensation on solids.

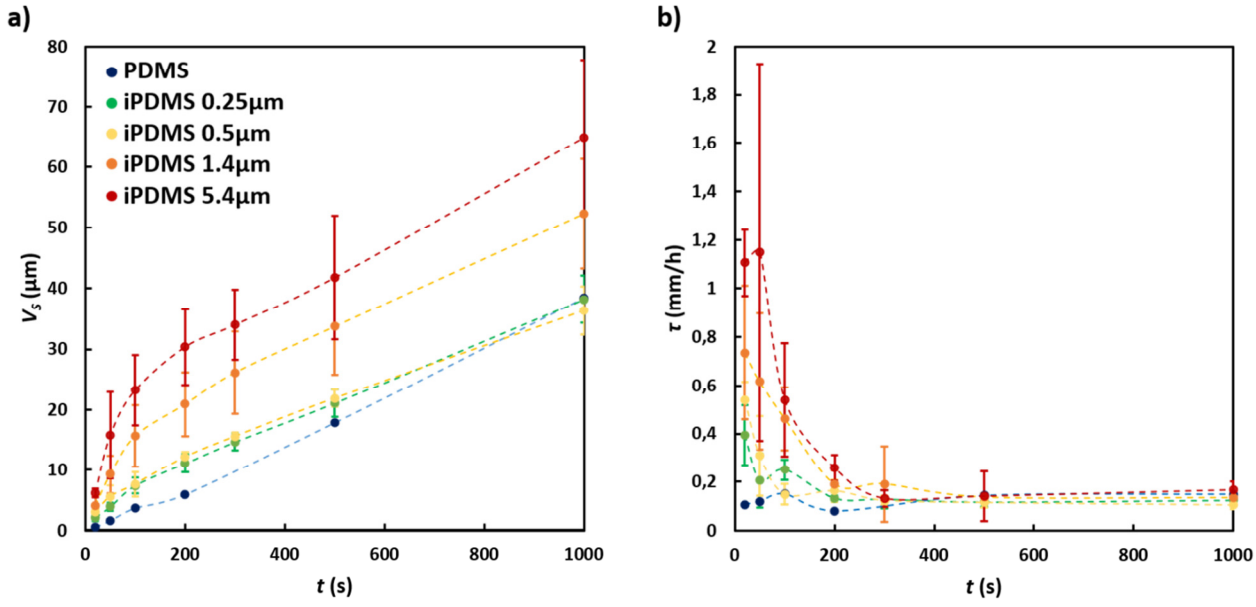

Figure 6: Condensed water volumes and condensation rates for PDMS and iPDMS horizontal surfaces with different oil layer thicknesses (0.25; 0.5; 1.4 and 5.4 µm): (a) Evolution of the total volume of condensed water per surface area V_s as a function of time, from the beginning of condensation. (b) Evolution of the condensation rate τ in mm.h.$^{-1}$. The error bars represent the standard deviation of triplicate experiments for each oil thickness (dotted curves are plotted between data points for visualization purpose).

(ii) Gravity-induced droplets shedding and collected water volumes

To assess the potential of iPDMS materials for heat transfer or water harvesting applications, gravity-induced shedding of condensed droplets is essential. For inclined surfaces, shedding starts when the droplet weight overcomes the pinning forces. Hence, low contact angle hysteresis (*CAH)* is key to minimize the critical droplet size (r_c) for gravity-induced shedding. In addition, shedding droplets clear the surface by sweeping all droplets in their trajectories, which leave additional free space for fresh nucleation and a subsequent, additional increase of condensation. The latency time for shedding, t_L *, is* defined as the time needed to observe the first droplet shedding event after the beginning of condensation. A coarsening process is thus an efficient route to minimize t_L, as it favors the differential growth of some large droplets that reach rapidly the critical radius r_c [20].

The movie S3 shows a condensation experiment on PDMS and a typical iPDMS, placed side by side on a vertical surface. On PDMS, the first droplet shedding is observed at a latency time t_L = 60 min with r_c > 500 µm. In the case of iPDMS, a much more rapid coarsening is observed than for PDMS, in agreement with the previous results. The first shedding occurs for a critical radius ≈ 100 µm after a latency time t_L of only 5 min. Droplets are constantly sliding down after this first shedding event. Droplet shedding, by continuously refreshing the surface, thus authorizes a novel cycle of nucleation – growth – shedding. After $t_L \approx$ 5 min. for iPDMS-2µm, a new cycle takes place with a fresh surface, higher condensation rate and thus larger collected volumes. The movie S4 shows condensation on iPDMS- 2µm where nucleation and high droplets mobility can be observed in the tracks of the sliding droplets.

Condensation experiments were performed over 4h on PDMS and iPDMS (with *h* ranging from 20 nm to 4 µm, calculated from Figure 1b) on vertical surfaces in a climatic chamber. To show the robustness of iPDMS material, the same sample was used for all the experiments in the climatic chamber. The sample was washed under water after each condensation experiment to remove the residual oil layer. The sample then was put at rest for spontaneous release of a new oil layer.

Figure 7 presents the time evolution of the mass of water collected at the bottom of the vertical surface and weighed along a 4 hours-lasting condensation experiment. Time is set to zero from the beginning of condensation on the surface, whereas water collection starts at a latency time t_L , measured here as the first time a drop is collected and weighed. Inset focuses on the first 5000 s (1.4 h) after the beginning of condensation. The most striking observation is that t_L is greatly influenced by the presence of the oil layer. This time gradually decreases with increasing oil thickness (Figures 7 and 8), ranging from 1 h. for PDMS to only 5 min. for iPDMS-4µm. Whereas a minimum oil thickness (0.25 µm) was shown to be sufficient to minimize *CAH,* the critical drop shedding radius is reached sooner with the increase of *h*, as a result of the coarsening effect being enhanced by the oil thickness.

When carefully looking on Figure 7, it can be observed that the evolution of the collected mass for PDMS proceeds by discrete steps. The steps are typical of the high hysteresis of PDMS surface, combined with a homogeneous growth droplet with time. As a result, water accumulates on the surface before the first drop reaches the critical radius, slides down and sweeps a large amount of water. Going from iPDMS-0.02µm to iPDMS-4µm, the steps progressively disappear and evolve towards a smooth and continuous collection. This smooth mass collection without steps is characteristic not only of an ultra-low hysteresis but also of the coarsening process. The condensation rates, defined as the slopes of the curves, are essentially the same at long time (after 10^4s) on all iPDMS surfaces and equal to ~5.10^{-4} g/s, corresponding to 0.2 mm/h. This is a consequence of an oil thickness reaching a minimum value on all samples at these long times. At very short times, however (500 s after collection begins), the condensation rates are larger than the steady-state value of 5.10^{-4} g/s , and this effect is more visible for shorter latency times (see inset in Figure 7). On a vertical surface, the first steps of condensation are not captured, because of the presence of a shedding latency time. Nevertheless, this short-time enhanced collection rate is consistent with the short-time enhanced condensation due to continuous nucleation process, as evidenced on horizontal surfaces. To show the repeatability of this set of experiments, three similar *h* values (0.4, 0.5 and 0.5 µm) were studied, resulting in three curves that almost superimpose.

It is important to note that the collected mass is not the whole condensed mass, some water volume remaining on the surface due to the different shedding delay times. Figure 8 gives the collection rate, τ_c , defined as the total volume of collected water per surface area, divided by total time elapsed from the beginning of condensation. It increases with larger oil thickness, not only because of shorter latency time, but also as a result of larger collection rates in the first seconds following the onset of collection, as explained above.

Figure 9 presents the mass percentage of oil in the collected water. Larger initial oil amount results in a larger mass percentage of oil in water, with a maximum found at around 0.1% for iPDMS-4µm after 4 h of condensation.

Finally, and remarkably, Figure 7 confirms the presence of a minimum oil layer thickness all along the 4 h. of condensation experiments, despite the fact that sweeping droplets drain a certain amount of oil. Indeed, in the presence of water droplet on the iPDMS, the minimization of surface energy requires the cloaking of the water droplets with oil. This cloaking process continuously "pumps" oil from the bulk matrix[33,34]. Thus, the process of condensation itself, by continuously extracting oil from the iPDMS, keeps a minimal oil thickness on the surface that suffices to sustain the beneficial properties of the iPDMS surface towards water condensation and collection.

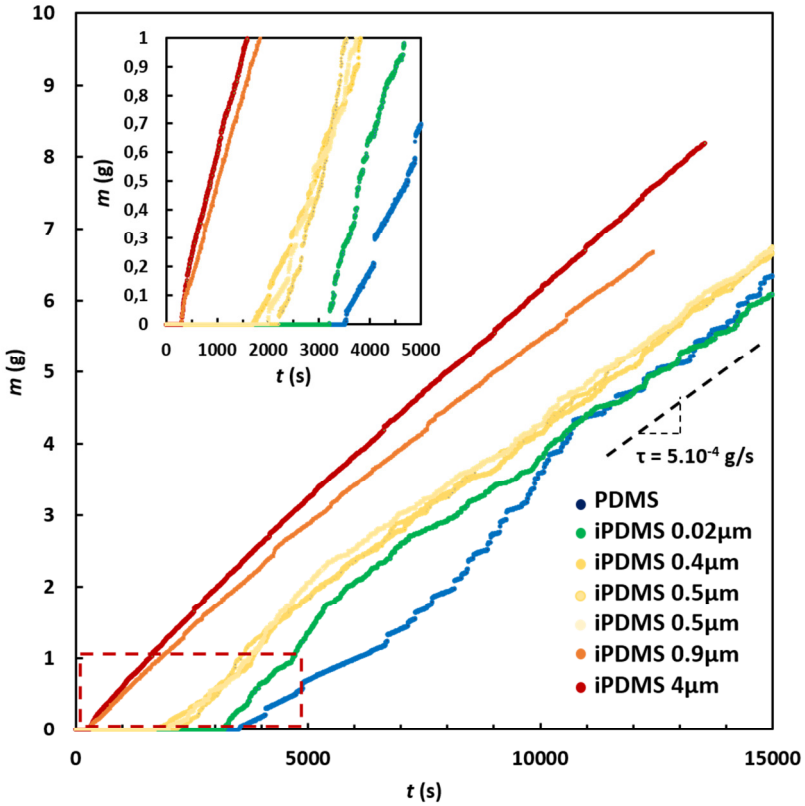

Figure 7: Collection of condensed water on vertical surfaces: Evolution of the mass of the collected water for PDMS and iPDMS with different oil layer thicknesses (0.02, 0.4, 0.5, 0.5, 0.9 and 4 µm) as a function of time from the beginning of condensation. The inset focuses on the first 5000 s (1.4 h) of the experiments. Condensation rate at large time of 5.10^{-4} g/s, is represented by the dotted black straight line.

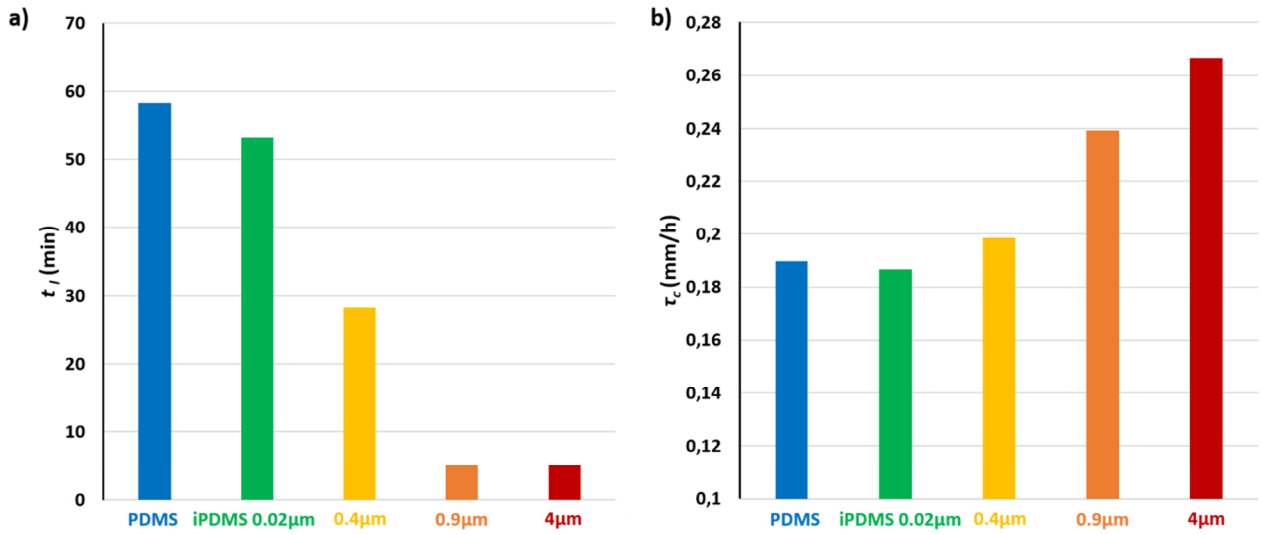

Figure 8: Water collection ability of iPDMS: (a) Latency time for droplet shedding, t_l , in min. and (b) collection rate, τ_c , expressed in volume of the collected water per surface area and time for PDMS and iPDMS of various oil thicknesses.

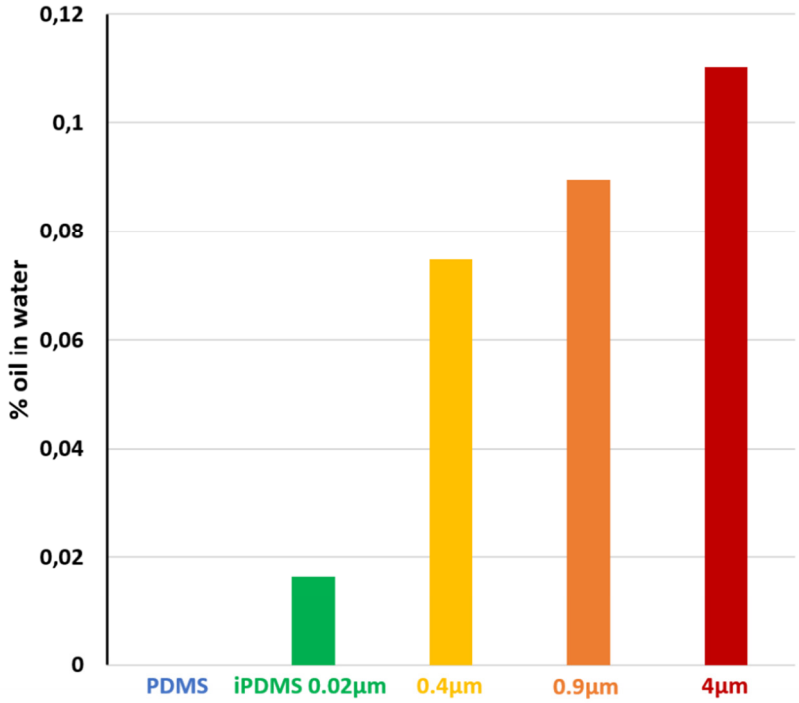

Figure 9: Mass percentage of oil in collected water for iPDMS of various initial oil thicknesses.

4. Conclusion and outlook

A layer of silicone oil is present at the surface of iPDMS, whose thickness slowly increases with time. Upon depletion, this layer is spontaneously renewed from the bulk matrix to minimize the surface energy. During the first seconds of water condensation, continuous nucleation proceeds within the oil layer. Further nucleation continues to take place on the oil surface left free by menisci-mediated coalescences or in the trace of shedding droplets. In contrast, on PDMS and usual solid substrates, contact-triggered coalescences do not free enough surface for re-nucleation at early times. Nucleation is thus hampered by the overlap of water molecule concentration profiles in between droplets. On a horizontal surface, it is shown that the continuous mechanism of water nucleation adds to the diffusive growth of the cloaked droplets whose surface remains permeable to water vapor molecules. On a vertical surface, the rapid growth of water droplets enhanced by meniscus mediated coalescences, and the ultra- low contact angle hysteresis, make the latency time for shedding very small.

The thickness of the oil layer can be controlled, and its influence on the above phenomena systematically quantified. For an oil layer of 5 μm, an increase of an order of magnitude of the condensation rate was measured in the first seconds of condensation, and almost twice more water volumes were measured after 1000 s of condensation compared with conventional solid PDMS surface. On a vertical surface, the latency time for droplet shedding is reduced from 1 h. to 5 min. and the amount of collected water increased by +50% after 4h of condensation, when the oil layer thickness is increased from 0.02 μm to 4 μm.

These performances make iPDMS a promising candidate for low heat transfer resistance or enhanced water production in industrial water condensation applications. The fabrication process is easily scalable at low cost, and the material shows robustness thanks to the self-healing of the oil layer over time due to residual crosslinking reactions within the solid PDMS matrix. Radiative sky cooling for natural dew harvesting could also be considered because of its high emissivity (> 0.9) in the atmospheric window[43]. Micro-patterning of PDMS could further enhance emissivity[43,44] and reduce oil drainage[30]. However, in view of using iPDMS in outdoor applications, care must be taken to its thermo-mechanical properties, as variations of volume may influence the oil release.

Redistribution of the oil around water droplets and their shedding decrease the oil layer thickness with time. However, thanks to the reservoir of oil within the crosslinked matrix, the energy minimization implies the spontaneous formation of a persistent minimum layer of oil on the surface of iPDMS, which is not the case for 2D-LIS materials. Upon shedding by gravity, water droplets, indeed, drain oil, which could deteriorate the quality of the collected water even if the oil concentration is quite low. Although spontaneous oil-water separation can be simply carried out by phase sedimentation, the release of oil and its impact on the environment has nevertheless to be carefully considered. Bio-based lubricants (extracted from plant oils) have been successfully used to infuse porous films by capillary wicking[45,46], a process different from polymer swelling. We expect that future research will focus on advancing the design of infused bio-based polymer networks as an environmental-friendly alternative to iPDMS.

Acknowledgements

This project received the support from the METAWATER Project (No. ANR-20-CE08-0023 META-WATER). The authors thank the IPGG (Institut Pierre-Gilles De Gennes) clean room facility for the preparation of the samples.

Conflict of Interest

The authors declare no conflict of interest.

References:

1 A. J. Hill, T. E. Dawson, O. Shelef and S. Rachmilevitch, *Oecologia*, 2015, **178**, 317–327.
2 S. Munné-Bosch and L. Alegre, *Journal of Plant Physiology*, 1999, **154**, 759–766.
3 A. R. Parker and C. R. Lawrence, *Nature*, 2001, **414**, 33–34.
4 D. J. Preston, Z. Lu, Y. Song, Y. Zhao, K. L. Wilke, D. S. Antao, M. Louis and E. N. Wang, *Sci Rep*, 2018, **8**, 540.
5 X. Zhao, G. Wu, J. Qi, M. to Baben and M. Müller, *Fuel*, 2021, **295**, 120600.
6 A. D. Khawaji, I. K. Kutubkhanah and J.-M. Wie, *Desalination*, 2008, **221**, 47–69.
7 D. Beysens, *Dew water*, River Publishers, Gistrup, Aalborg, Denmark, 2018.
8 A. Lee, M.-W. Moon, H. Lim, W.-D. Kim and H.-Y. Kim, *Langmuir*, 2012, **28**, 10183–10191.
9 X. Liu, D. Beysens and T. Bourouina, *ACS Materials Lett.*, 2022, **4**, 1003–1024.
10 S. Anand, A. T. Paxson, R. Dhiman, J. D. Smith and K. K. Varanasi, *ACS Nano*, 2012, **6**, 10122–10129.
11 J. Sun and P. B. Weisensee, *Soft Matter*, 2019, **15**, 4808–4817.
12 A. Lafuma and D. Quéré, *EPL*, 2011, **96**, 56001.
13 T.-S. Wong, S. H. Kang, S. K. Y. Tang, E. J. Smythe, B. D. Hatton, A. Grinthal and J. Aizenberg, *Nature*, 2011, **477**, 443–447.
14 R. Xiao, N. Miljkovic, R. Enright and E. N. Wang, *Sci Rep*, 2013, **3**, 1988.
15 K. Rykaczewski, A. T. Paxson, M. Staymates, M. L. Walker, X. Sun, S. Anand, S. Srinivasan, G. H. McKinley, J. Chinn, J. H. J. Scott and K. K. Varanasi, *Sci Rep*, 2015, **4**, 4158.
16 F. Eslami and J. A. W. Elliott, *J. Phys. Chem. B*, 2011, **115**, 10646–10653.
17 M. Sokuler, G. K. Auernhammer, M. Roth, C. Liu, E. Bonacurrso and H.-J. Butt, *Langmuir*, 2010, **26**, 1544–1547.
18 S. Anand, K. Rykaczewski, S. B. Subramanyam, D. Beysens and K. K. Varanasi, *Soft Matter*, 2015, **11**, 69–80.
19 J. Sun, X. Jiang and P. B. Weisensee, *Langmuir*, 2021, **37**, 12790–12801.
20 Z. Guo, L. Zhang, D. Monga, H. A. Stone and X. Dai, *Cell Reports Physical Science*, 2021, **2**, 100387.
21 J. D. Smith, R. Dhiman, S. Anand, E. Reza-Garduno, R. E. Cohen, G. H. McKinley and K. K. Varanasi, *Soft Matter*, 2013, **9**, 1772–1780.
22 A. Keiser, L. Keiser, C. Clanet and D. Quéré, *Soft Matter*, 2017, **13**, 6981–6987.
23 A. Steyer, P. Guenoun and D. Beysens, *Phys. Rev. E*, 1993, **48**, 428–431.
24 M. J. Hoque, S. Sett, X. Yan, D. Liu, K. F. Rabbi, H. Qiu, M. Qureshi, G. Barac, L. Bolton and N. Miljkovic, *ACS Appl. Mater. Interfaces*, 2022, **14**, 4598–4611.
25 S. Peppou-Chapman, J. K. Hong, A. Waterhouse and C. Neto, *Chem. Soc. Rev.*, 2020, **49**, 3688–3715.
26 S. Adera, J. Alvarenga, A. V. Shneidman, C. T. Zhang, A. Davitt and J. Aizenberg, *ACS Nano*, 2020, **14**, 8024–8035.
27 H. Tsuchiya, M. Tenjimbayashi, T. Moriya, R. Yoshikawa, K. Sasaki, R. Togasawa, T. Yamazaki, K. Manabe and S. Shiratori, *Langmuir*, 2017, **33**, 8950–8960.
28 D. Seo, J. Shim, C. Lee and Y. Nam, *Sci Rep*, 2020, **10**, 2959.
29 N. MacCallum, C. Howell, P. Kim, D. Sun, R. Friedlander, J. Ranisau, O. Ahanotu, J. J. Lin, A. Vena, B. Hatton, T.-S. Wong and J. Aizenberg, *ACS Biomater. Sci. Eng.*, 2015, **1**, 43–51.
30 N. Lavielle, D. Asker and B. D. Hatton, *Soft Matter*, 2021, **17**, 936–946.

31 Q. S. Bhatia, J.-K. Chen, J. T. Koberstein, J. E. Sohn and J. A. Emerson, *Journal of Colloid and Interface Science*, 1985, **106**, 353–359.
32 K. Grundke, S. Michel, G. Knispel and A. Grundler, *Colloids and Surfaces A: Physicochemical and Engineering Aspects*, 2008, **317**, 598–609.
33 C. S. Sharma, A. Milionis, A. Naga, C. W. E. Lam, G. Rodriguez, M. F. Del Ponte, V. Negri, H. Raoul, M. D'Acunzi, H. Butt, D. Vollmer and D. Poulikakos, *Adv Funct Materials*, 2022, **32**, 2109633.
34 A. Hourlier-Fargette, A. Antkowiak, A. Chateauminois and S. Neukirch, *Soft Matter*, 2017, **13**, 3484–3491.
35 F. Peters and D. Arabali, *Colloids and Surfaces A: Physicochemical and Engineering Aspects*, 2013, **426**, 1–5.
36 A. E. Ismail, G. S. Grest, D. R. Heine, M. J. Stevens and M. Tsige, *Macromolecules*, 2009, **42**, 3186–3194.
37 D. Beysens, *Comptes Rendus Physique*, 2006, **7**, 1082–1100.
38 M.-G. Medici, A. Mongruel, L. Royon and D. Beysens, *Phys. Rev. E*, 2014, **90**, 062403.
39 D. Beysens, *The physics of dew, breath figures and dropwise condensation*, Springer, Cham, 2022.
40 M. Marcos-Martin, D. Beysens, J. P. Bouchaud, C. Godrèche and I. Yekutieli, *Physica A: Statistical Mechanics and its Applications*, 1995, **214**, 396–412.
41 P. Bian, Y. Wang and T. J. McCarthy, *Macromol. Rapid Commun.*, 2021, **42**, 2000682.
42 M. Sokuler, G. K. Auernhammer, C. J. Liu, E. Bonaccurso and H.-J. Butt, *Europhys. Lett.*, 2010, **89**, 36004.
43 E. Lee and T. Luo, *Solar Energy Materials and Solar Cells*, 2019, **194**, 222–228.
44 J. Song, J. Seo, J. Han, J. Lee and B. J. Lee, *Appl. Phys. Lett.*, 2020, **117**, 094101.
45 R. Mukherjee, M. Habibi, Z. T. Rashed, O. Berbert, X. Shi and J. B. Boreyko, *Sci Rep*, 2018, **8**, 11698.
46 M. Mikriukova, J. Lahti, J. Haapanen, J. M. Mäkelä and J. Kuusipalo, *Nordic Pulp & Paper Research Journal*, 2020, **35**, 479–489.

Supporting information

Supplementary note: Calculation of the amplitude constants *A* and *E*.

Inspired by references [40] and [42], the calculation of the amplitude constants *A* (condensation) and *E* (evaporation) can be expressed as follows:

$$A = E = \frac{4D(c_\infty - c_s)f(\Theta)}{3\rho_w sin\Theta\, G(\Theta)}$$

With:

$$f(\Theta) = \frac{1}{2}(0.00008957 + 0.6333\Theta + 0.116\Theta^2 - 0.08878\Theta^3 + 0.01033\Theta^4)$$

and

$$G(\Theta) = \frac{2 - 3cos\Theta + cos\Theta^3}{3sin\Theta^3}$$

D being the diffusion coefficient of water; c_∞, c_s the concentration of water monomers far and on the drop surface, respectively; ρ_w, the water density and *Θ*, the dynamic contact angle equal to Θ_a (advancing contact angle) in the case of the condensation and to Θ_r (receding contact angle) in the case of the evaporation.

As condensation (/ evaporation) experiments on iPDMS, PDMS and Si were performed in the same conditions, the only varying parameter is the geometrical argument (i.e. *f(Θ)*, *G(Θ)* and *sinΘ*) and the respective ratios of *A* and *E* were calculated and compared to the experimental values:

	PDMS	iPDMS	Si
Θ_a (°)	120	105	75
Θ_r (°)	60	105	55
$A_{theo.}$ (µm²/s)	0.41	0.57	0.97
$E_{theo.}$ (µm²/s)	1.26	0.57	1.39

	theo.	exp.
A_{iPDMS}/A_{PDMS}	1.4	3.8
A_{iPDMS}/A_{Si}	0.6	1.2
E_{iPDMS}/E_{PDMS}	0.5	0.5
E_{iPDMS}/E_{Si}	0.4	0.2

Table 1: Advancing / receding contact angles, theoretical amplitude constants (*A* for condensation, *E* for evaporation) and comparison between theoretical and experimental amplitude constants ratios for PDMS, iPDMS and Si.

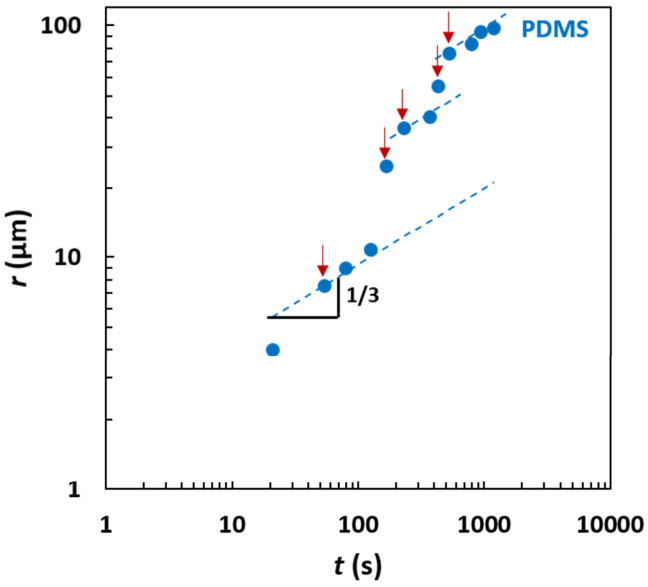

Supplementary Figure S1: Droplet growth on PDMS horizontal surfaces: Typical radius evolution of a single droplet on PDMS with time (coalescence events are indicated by red arrows).

a)

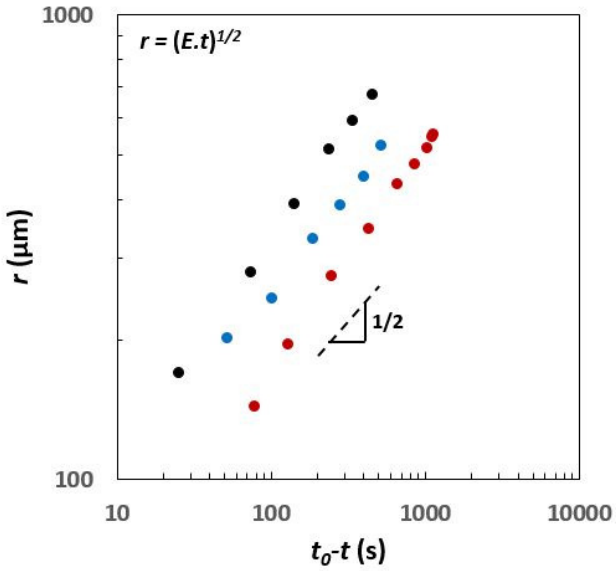

b)

Material	t_{evap} (s)	E (µm²/s)
iPDMS	1100	324
PDMS	950	625
Si	530	1369

Supplementary Figure S2: Evaporation of a deposited droplet on iPDMS, PDMS and Si surfaces: a) Radius evolution of 0.5µL water droplet as function of time (t_0-t, with t_0 the time of droplet disappearance). b) Time needed for the water droplet to completely evaporate and related values of E.

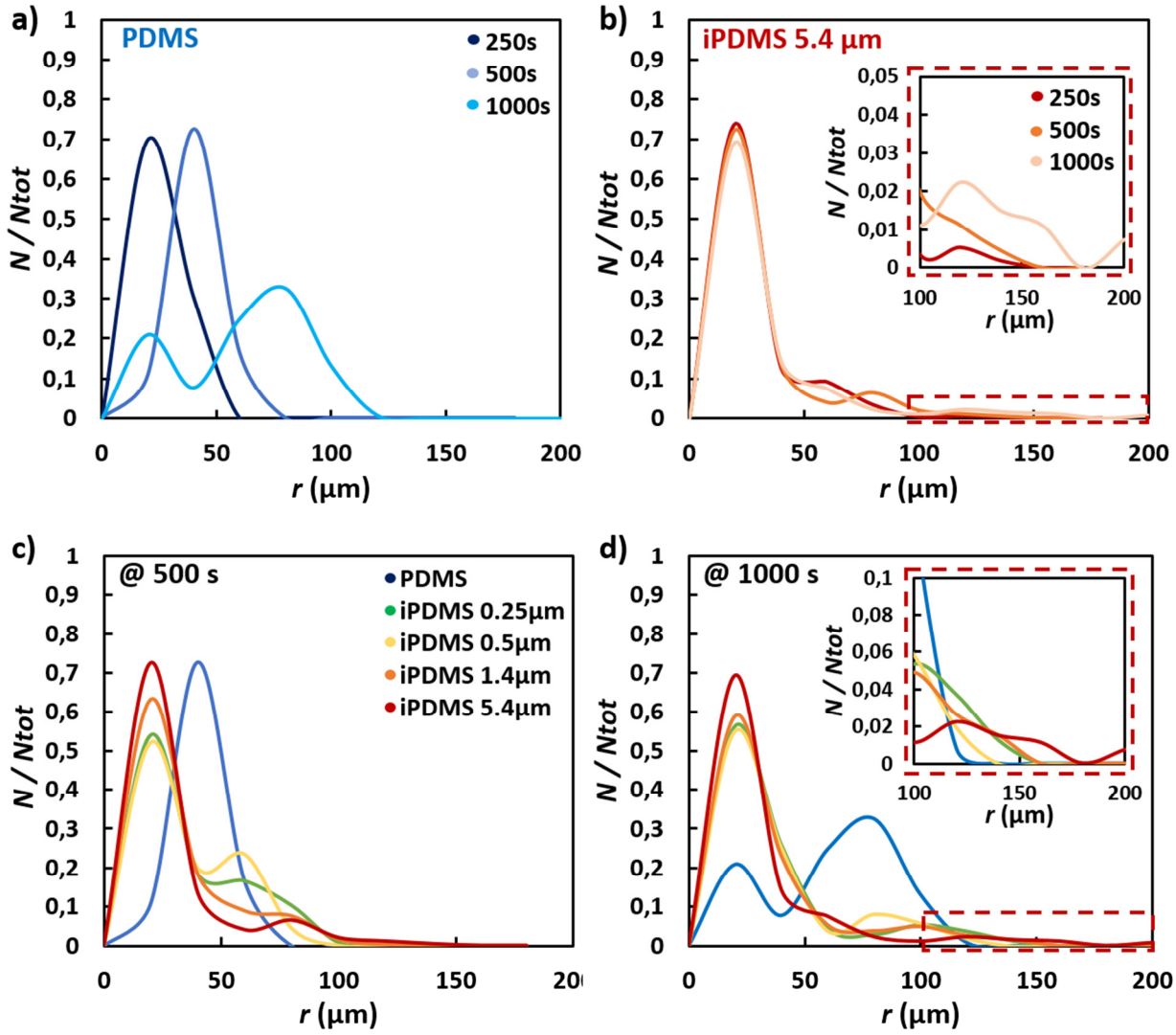

Supplementary Figure S3: Normalized radius distribution of condensed water droplets on horizontal surfaces: Evolution of the number of droplets, *N*, of radius *r*, for (a) PDMS and (b) iPDMS with 5.4µm oil thickness. Normalized size distribution for PDMS and iPDMS with various oil thicknesses at (c) 500 s and (d) 1000 s. (Step of 20 µm).

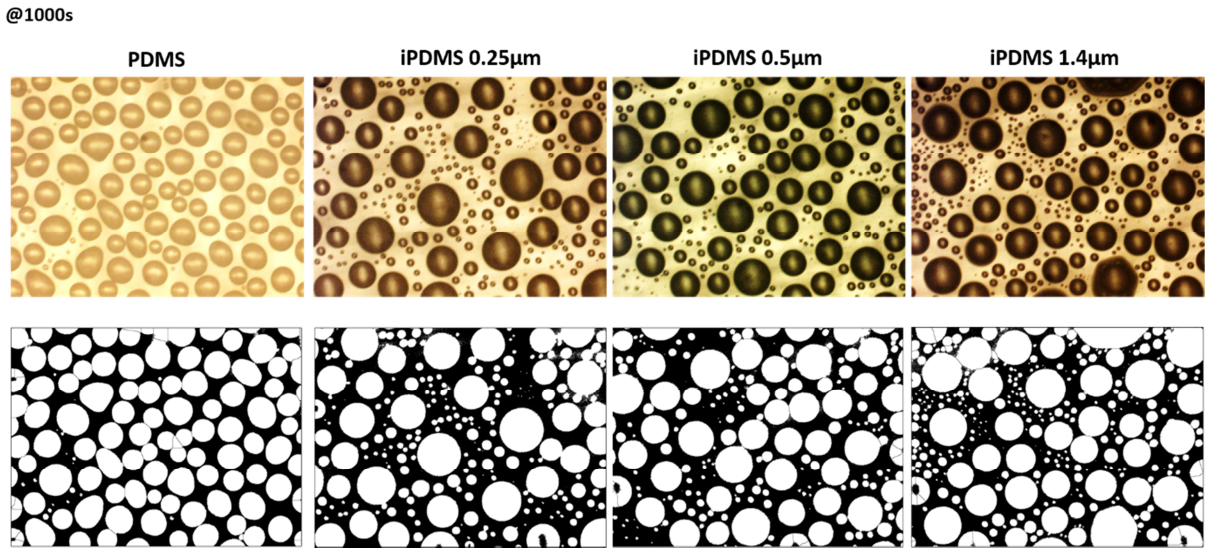

Supplementary Figure S4: **Microscope images for PDMS, iPDMS (0.25, 0.5 and 1.4um)**: Corresponding threshold images at 1000 s of condensation. The periphery of each droplet is well defined and only a few (2 or 3) drops display a visible wetting ridge for iPDMS 1.4um.

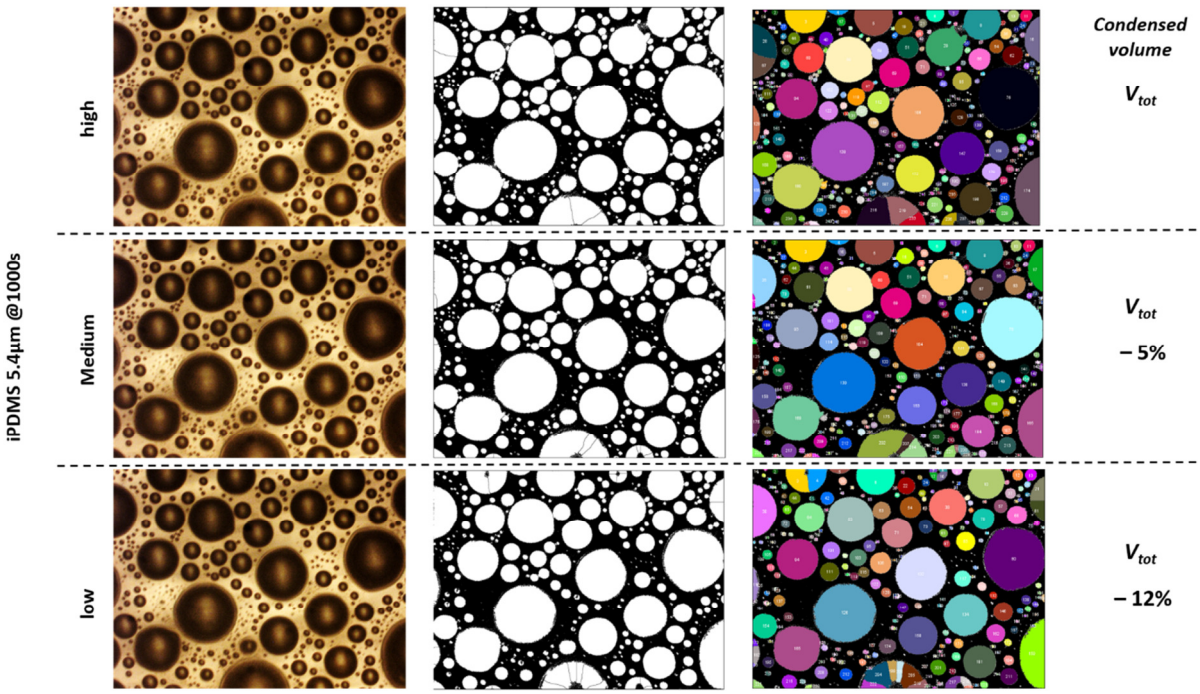

Supplementary Figure S5: **Microscope image for iPDMS 5.4um at 1000s of condensation**: Comparison of the corresponding image analysis with low, medium and high threshold for removing the influence of the wetting ridge in the determination of the drop volumes.